ory based on low polar temperatures) because most of the crater floor would be in perpetual shadow.

REFERENCES AND NOTES

1. For circularly polarized transmission, the polarized echo is the component returned in the circular polarization orthogonal to the transmitted sense; the depolarized echo is the component returned in the same polarization sense. The polarized echo is normally dominated by quasi-specular reflection from large planar facets in the near-subradar region. The depolarized echo can be associated with diffuse reflection from wavelength-scale roughness elements, multiple scattering, or subsurface scattering in icy regoliths.
2. S. Zohar and R. M. Goldstein, *Astron. J.* **79**, 85 (1974).
3. P. E. Clark, M. A. Leake, R. F. Jurgens, in *Mercury*, F. Vilas, C. R. Chapman, M. S. Matthews, Eds. (Univ. of Arizona Press, Tucson, 1988), pp. 77–100.
4. A radar target is said to be "overspread" when the product $B\tau$ of its rotational Doppler bandwidth B and delay depth τ exceeds unity. Conventional delay-Doppler mapping uses a repetitive code with a cycle time greater than τ. Because the sampling interval for the spectral (Doppler) analysis is equal to the code cycle time, the echo from an overspread target will be aliased in Doppler. Mercury is overspread by up to 75% at S-band wavelengths and 270% at X-band wavelengths.
5. M. A. Slade, B. J. Butler, D. O. Muhleman, *Science* **258**, 635 (1992).
6. J. K. Harmon, M. P. Sulzer, P. J. Perillat, J. F. Chandler, *Icarus* **95**, 153 (1992).
7. The decoding for a given delay bin is done by multiplication of the echo signal by an appropriately lagged replica of the transmitted code. The uncorrelated product of the code and the echo from other delays constitutes a random "clutter" that adds to the total noise background. For more on this coding technique, see M. P. Sulzer [*Radio Sci.* **21**, 1033 (1986)].
8. R. M. Goldstein, *Science* **168**, 467 (1970).
9. G. H. Pettengill and T. W. Thompson, *Icarus* **8**, 457 (1968).
10. T. W. Thompson, *Moon* **10**, 51 (1974).
11. D. O. Muhleman, B. J. Butler, A. W. Grossman, M. A. Slade, *Science* **253**, 1508 (1991).
12. S. H. Zisk, G. H. Pettengill, G. W. Catuna, *Moon* **10**, 17 (1974).
13. J. K. Harmon, D. B. Campbell, D. L. Bindschadler, J. W. Head, I. I. Shapiro, *J. Geophys. Res.* **91**, 385 (1986).
14. K. P. Klaasen, *Icarus* **28**, 469 (1976).
15. M. E. Davies, S. E. Dwornik, D. E. Gault, R. G. Strom, *Atlas of Mercury* (National Aeronautics and Space Administration, Washington, DC, 1978).
16. R. M. Killen, A. E. Potter, T. H. Morgan, *Icarus* **85**, 145 (1990).
17. B. Hapke, *ibid.* **88**, 407 (1990).
18. A. L. Broadfoot, *Rev. Geophys. Space Phys.* **14**, 625 (1976).
19. D. A. Paige, S. E. Wood, A. R. Vasavada, *Science* **258**, 643 (1992).

20. A. Crespo, R. Vélez, J. Cruz, A. Vázquez, P. Perillat, M. Dryer, M. Sulzer, and J. Chandler provided support for the Arecibo observations. We thank the authors of the companion papers (D. Paige, S. Wood, A. Vasavada, B. Butler, and D. Muhleman) for communicating some of their results to us before publication. Part of the research described above was carried out by the Jet Propulsion Laboratory, California Institute of Technology, under contract with the National Aeronautics and Space Administration (NASA). The National Astronomy and Ionosphere Center (Arecibo Observatory) is operated by Cornell University under a cooperative agreement with the National Science Foundation and with support from NASA.

29 May 1992; accepted 20 July 1992

The Thermal Stability of Water Ice at the Poles of Mercury

David A. Paige,* Stephen E. Wood, Ashwin R. Vasavada

Recent radar observations of Mercury have revealed the presence of anomalous radar reflectivity and polarization features near its north and south poles. Thermal model calculations show that, despite Mercury's proximity to the sun, the temperatures of flat, low-reflectivity surfaces at Mercury's poles are not expected to exceed 167 kelvin. The locations of the anomalous polar radar features appear to be correlated with the locations of large, high-latitude impact craters. Maximum surface temperatures in the permanently shadowed regions of these craters are expected to be significantly colder, as low as 60 kelvin in the largest craters. These results are consistent with the presence of water ice, because at temperatures lower than 112 kelvin, water ice should be stable to evaporation over time scales of billions of years.

Over the past three decades, a circumstantial case has developed for the possible stability of water ice deposits in high-latitude, permanently shadowed regions on the moon (*1–3*), but there is no definitive observational evidence for their existence. The possibility that water ice could be cold-trapped at the poles of Mercury has also been suggested (*4*). The new 3.5-cm (*5*) and 12.6-cm (*6*) radar observations of Mercury motivate detailed consideration of the thermal state of the planet's polar regions as well as the long-term sources and sinks of water and other volatiles (*7*). Here we report the results of thermal model calculations that suggest that water ice could be stable to evaporation on Mercury in regions where anomalous radar reflectivity and polarization features are observed.

Using a thermal model, we have calculated the temperatures of flat surfaces on Mercury as a function of latitude, longitude, and season. Because of Mercury's 3/2 resonant rotation rate and eccentric orbit, the distribution of incident solar radiation is a complicated function that repeats every 2 years (*8*). Because of the planet's proximity to the sun, the finite angular size of the sun's disk (*9*) and solar limb darkening are taken into account when the sun's disk intersects the local horizon. Near Mercury's poles, the distribution of incident solar radiation is sensitive to the orientation of the planet's rotation axis relative to its orbital plane. Recent Arecibo radar observations show that Mercury's obliquity is less than 1° (*6*). Dynamical models predict that the most stable configuration of Mercury's spin axis corresponds to Cassini State 1, in which the spin axis is displaced slightly away from the orbit normal vector in a direction that is coplanar with the solar system normal vector and the orbit normal vector (*10*). The magnitude of this displacement is determined by the differences in the principal moments of inertia (*10*). Based on Mariner 10 gravity data (*11*), the present obliquity of Mercury is likely to be $\leq 0.05°$ (*10*). In our model, the Cassini State 1 configuration is assumed; in it, northern spring equinox occurs at the ascending node of Mercury's orbit relative to the solar system plane (*12*). The present value of ω, the angle between the ascending node and perihelion, is approximately 29.1° (*13*).

Because Mercury lacks an appreciable atmosphere, we determined the temperatures of flat surfaces using only the net effects of solar and infrared radiation and thermal conduction. Ground-based observations and Mariner 10 data have shown that the average thermal and reflectance properties of the surface of Mercury are similar to those of the moon (*14, 15*). In our model, the solar reflectance of the surface was assumed to be 0.15 and the emissivity of the surface was assumed to be 0.90. At each latitude and longitude, the model solves the one-dimensional heat diffusion equation using the bulk thermal properties of lunar soil, including the expected variation of thermal conductivity and heat capacity with temperature (*16*). In accordance with the results of models for the thermal history of Mercury's interior, the present surface heat flow rate was assumed to be 0.020 W/m^2 (*17*). The general results of the model calculations were consistent with those of earlier studies in that daytime surface temperatures were close to being in instantaneous radiative equilibrium and nighttime surface temperatures were determined by the combined effects of thermal inertia and heat flow (*8, 14*).

Maps of model-calculated, biannual maximum and average temperatures for flat surfaces in the north polar region of Mercury (Fig. 1, A and B) show strong longitudinal dependence. Because noon at perihelion occurs alternately at longitudes of 0° and 180°, polar isotherms tend to be elon-

Department of Earth and Space Sciences, University of California, Los Angeles, Los Angeles, CA 90024.

*To whom correspondence should be addressed.

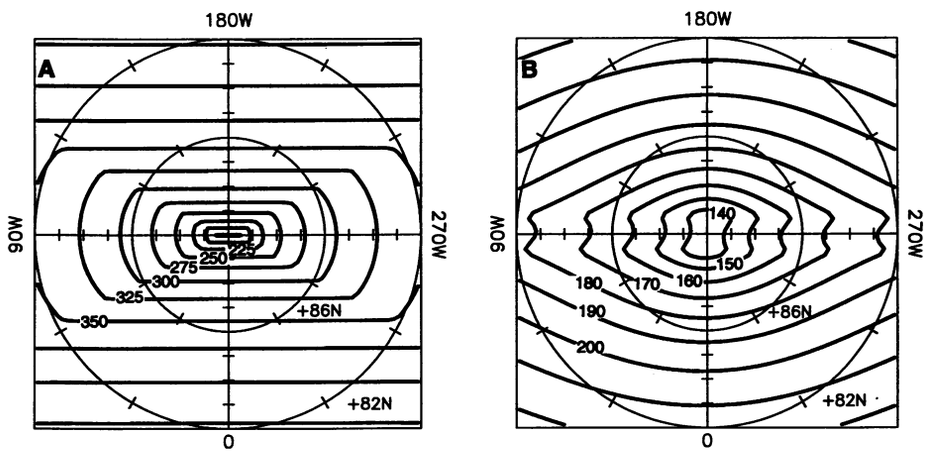

Fig. 1. Model-calculated biannual (**A**) maximum and (**B**) average temperatures (in kelvins) for flat surfaces in Mercury's north polar region. Water ice vacuum evaporation rates <1 m per billion years would require temperatures of less than 112 K.

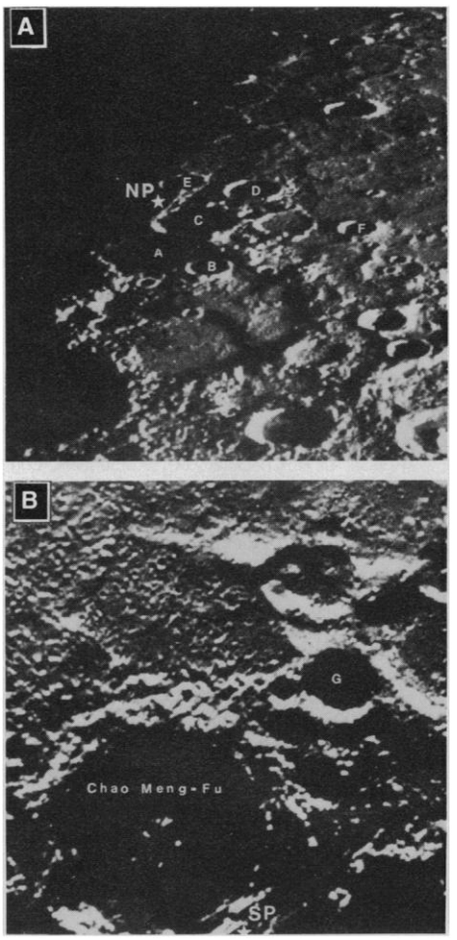

Fig. 2. Mariner 10 images of the (**A**) north and (**B**) south polar regions of Mercury. Both images were acquired when the subsolar latitude was at the equator and the subsolar longitude was close to 100°W. The center latitudes and center longitudes of the large impact craters labeled A to G and Chao Meng-Fu are listed in Table 1. NP, north pole; SP, south pole. Substantial portions of the interiors of these craters are permanently shadowed.

gated along the 90° to 270° meridian, which always experiences dawn or dusk during perihelion passage. The small enhancements in annual average temperatures near longitudes of 90° and 270° arise because Mercury's orbital angular velocity exceeds its rotational angular velocity near perihelion, which results in a brief second sunrise or sunset at these longitudes. Calculated temperatures decrease sharply toward the pole but remain well above minimum nighttime temperatures at lower latitudes because at the poles, a large fraction of the sun's disk remains above the horizon throughout the year. The biannual maximum surface temperature at the poles was 167 K. The biannual average surface temperature at the poles was 138 K. Calculated biannual average surface temperatures are lower limits for the temperatures of soil layers below the penetration depth of the biannual temperature wave, which is approximately 11 cm.

Based on the results of lunar studies, model-calculated temperatures (Fig. 1, A and B) are too high to permit the stability of water ice or any other more volatile substance for extended periods. Watson *et al.* (*1*) have estimated that, if lunar cold traps had maximum temperatures of 120 K, then water ice evaporation rates in these regions would be less than 1 m per billion years. Using recent vapor pressure measurements for crystalline ice obtained at temperatures as low as 131.8 K (*18*), we estimate that vacuum evaporation rates of less than 1 m per billion years would require temperatures of less than 112 K (*19*). In reality, the temperatures required for ice stability depend on water supply rates as well as loss rates due to other processes (*2*, *7*). However, because equilibrium vapor pressures increase rapidly with temperature, low temperatures are a necessary precondition for the stability of water ice on Mercury. For instance, at 131.8 K the vacuum evaporation rate of crystalline ice is over 2 km per billion years (*20*).

We investigated the sensitivity of the results of our flat-surface thermal model to potential variations in radiative and orbital parameters. As the argument of perihelion precesses, the longitudes that experience the lowest annual average temperatures can shift. For the present value of ω, the long axis of the annual average temperature contours is rotated toward the 240° to 60° meridian in the northern hemisphere and toward the 300° to 120° meridian in the southern hemisphere. The long axis of the annual maximum temperature contours in each hemisphere is slightly rotated in the opposite direction, but this effect is barely detectable for an obliquity of 0.05°, as is assumed for Fig. 1, A and B. Increasing the obliquity results in more noticeable rotation effects but also results in generally higher average and maximum temperatures in both polar regions. In the flat-surface model, the only parameter that can substantially decrease calculated polar temperatures is the solar reflectivity of the surface. For an obliquity of 0.05°, we found that to achieve annual average temperatures of 112 K at the poles requires surface reflectivities of 0.66. Achieving annual maximum temperatures of 112 K requires surface reflectivities of 0.83. The measured, spectrally integrated reflectivities of terrestrial snow deposits at high solar incidence angles can range from 0.85 to 0.97 (*21*). Thus, exposed surface ice deposits could potentially be stable at Mercury's poles, but only if they maintain high reflectivities. Ground ice deposits could also be stable in regions with unusually high soil reflectivities. Polar soil reflectivities of 0.66 may not be inconceivable on Mercury, given that anomalous bright patches with reflectivities as high as 0.45 are observed at lower latitudes (*14*). Under certain circumstances, the total reflectivities of particulate surfaces can be significantly enhanced at high solar incidence angles (*22*). Models for the lunar surface that can reproduce disk-integrated lunar brightness measurements (*23*) predict that, at solar incidence angles of 85°, the total reflectivity of the lunar surface is higher than the reflectivity at normal incidence by almost a factor of 2 (*22*).

Because surfaces near Mercury's poles are always illuminated at large solar incidence angles, topographic features are likely to have significant effects on surface temperatures. Mariner 10 images of Mercury's north and south polar regions (Fig. 2, A and B) show no obvious surface ice deposits, but they do show impact craters (*24*). The approximate locations and dimensions of eight high-latitude craters are

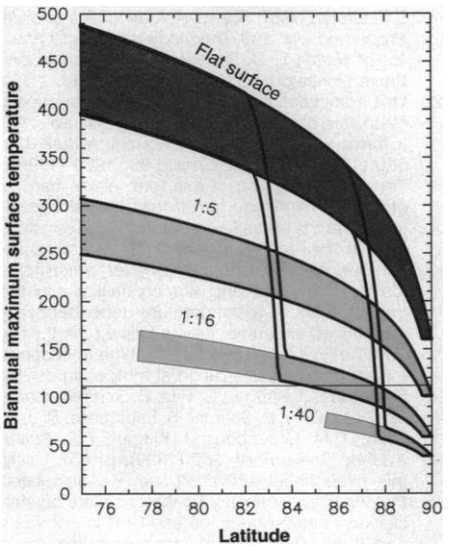

Fig. 3. Model-calculated biannual maximum temperatures (in kelvin) as a function of latitude for flat surfaces on Mercury, for surfaces at the centers of craters, and for surfaces in permanently shadowed portions of craters. Results for crater depth-to-diameter ratios of 1:5, 1:16, and 1:40 are shown. Ratios of 1:5 are characteristic of simple bowl-shaped craters with diameters of less than ~10 km; ratios of 1:16 are characteristic of more complex craters with diameters of ~25 km; and ratios of 1:40 are characteristic of mature complex craters and proto-basins with diameters of ~150 km (*28*). The upper and lower boundaries of the shaded areas show the range of maximum temperature variation with longitude. The upper boundaries indicate maximum temperatures at the 0° to 180° meridian, which experiences noon at perihelion, and the lower boundaries indicate maximum temperatures at the 90° to 270° meridian, which experiences noon at aphelion. The percentage of permanently shadowed area in craters with depth-to-diameter ratios of 1:5, 1:16, and 1:40 approaches zero at latitudes of 50°, 77.5°, and 85.5°, respectively. Biannual maximum surface temperatures at the centers of craters, which are almost the same as flat surface temperatures at low latitudes and are equal to permanently shadowed temperatures near the poles, are indicated by thick black lines. Craters with regions that never exceed 112 K are expected only within ~5° of the poles. Large, shallow craters are the most likely locations for thermally stable ice deposits because they contain the coldest permanently shadowed terrain.

Table 1. High-latitude impact craters on Mercury as indicated in Fig. 2.

Crater	Center latitude	Center longitude	Diameter (km)
A	87.7	174	90
B	86.8	167	30
C	89.1	131	55
D	88.5	67	40
E	88.7	12.5	30
F	86.6	137	25
G	84.8	78	50
Chao Meng-Fu	87.5	130	155

listed in Table 1. Given Mercury's low obliquity, it is clear from these images that substantial portions of the interior regions of these craters are permanently shadowed. We developed a model that estimates biannual maximum surface temperatures in high-latitude craters that is analogous to models that have been used to estimate the temperatures of permanently shadowed regions on the moon (*1–3*). The temperature at each location in the crater was determined by an instantaneous balance between the rates of absorption of direct solar radiation (including the effects of the angular size of the sun's disk); absorption of multiply scattered solar radiation within the crater; emission of blackbody radiation and absorption of reradiated blackbody radiation in the crater; and heat flow from Mercury's interior. The interior surfaces of craters were represented by sections of spheres, which makes it possible to analytically calculate surface heating rates due to multiply scattered sunlight and reradiated infrared radiation (*3, 25, 26*). Because lateral heat conduction effects can be ignored, the calculated surface temperatures are independent of the crater size. Because of the spherical geometry, all surfaces that are completely shadowed at a given time in a given crater have the same temperature. We assume that all crater surfaces have solar reflectivities of 0.15 and infrared emissivities of 1.0. Shadow-length measurements of a large sampling of impact craters on Mercury reveal a clear progression of crater shape profiles as a function of crater diameter, with larger craters having smaller depth-to-diameter ratios (*27*). We used three depth-to-diameter ratios to represent the range of crater morphologies found in Mercury's polar regions (see legend to Fig. 3).

Our results show that maximum temperatures in the shadowed regions of high-latitude craters on Mercury can be substantially colder than those calculated for flat surfaces (Fig. 3). Maximum temperatures of surfaces at crater centers that are completely illuminated at noon are almost exactly the same as those of flat surfaces at the same latitude. Maximum surface temperatures at crater centers that are partially illuminated at noon decrease rapidly with increasing latitude. They become equal to maximum permanent shadow temperatures when crater rims prevent any direct illumination. The latitudes at which crater centers become permanently shadowed depend on crater depth-to-diameter ratios. The centers of smaller bowl-shaped craters, which have larger depth-to-diameter ratios, become permanently shadowed at lower latitudes. However, the steep walls of these craters reflect and reemit more radiation to their interiors, which results in increased annual maximum temperatures in shadowed regions. Therefore, as on the moon (*3*), maximum temperatures in the permanently shadowed regions of almost all small, bowl-shaped craters on Mercury are not likely to be cold enough to permit the stability of water ice for extended periods. Our calculations show that reemitted infrared fluxes inside all craters on Mercury should be much greater than reflected solar fluxes, so that even bright water ice deposits in smaller craters should not be stable. On the other hand, maximum temperatures in the permanently shadowed regions of larger, shallower craters are distinctly colder. Only craters located within 5° of the pole are predicted to contain substantial regions that never exceed 112 K. Large, shallow craters are the most likely locations for thermally stable ice deposits because they contain the coldest permanently shadowed terrain. The results of finite-element models suggest that the temperatures of permanently shadowed regions in more realistically shaped, flat-floored craters should be colder than those with spherical cross sections (*3*). Therefore, our estimates of temperatures in these regions may be upper limits.

Unless polar surfaces have unusually high reflectivities, possible water ice deposits on Mercury are likely to be confined to regions that are permanently shadowed by the rims of large impact craters or by similar topographic features. The results of the 3.5-cm (*5*) and 12.6-cm (*6*) radar measurements to date suggest a good correlation between the locations of anomalous radar reflectivity and polarization features and the locations of large, high-latitude impact craters. Both sets of measurements show anomalous features only at high polar latitudes. In the southern hemisphere, the 12.6-cm feature appears to be contained within the Chao Meng-Fu crater (*6*). In the northern hemisphere, at least in the areas of the planet that have been imaged by Mariner 10, the 3.5-cm and 12.6-cm features are also in regions that have many large impact craters (*5, 6*). Because of the small depth-to-diameter ratios of these craters and the inclination of Mercury's orbit relative to the ecliptic plane, the Earth-based radar-viewing geometry permitted observation of a large fraction of these craters' permanently shadowed terrain.

In total, the case for water ice at the poles of Mercury appears quite strong. Considerations of the optical and dielectric properties required to produce the observed anomalous radar reflectivity and polarization features show that they are most easily explained by coherent backscattering (*5–*

7), which is diagnostic of the presence of at least some kind of ice (5–7). There also appear to be many processes that can supply water to permanent cold traps on Mercury (7), and, as long as evaporation rates are sufficiently low, long-term ice stability should be maintained (7). Of all the volatile, ice-like substances in the solar system, crystalline water ice has the lowest vapor pressure at these temperatures by several orders of magnitude (28). This property, plus its high cosmic abundance, makes water ice the most likely material to be cold-trapped in Mercury's permanently shadowed regions. Other, less volatile substances should also be cold-trapped near Mercury's poles. However, if the presence of these other materials were the only explanation for the anomalous radar features, then it would be difficult to understand why they would only be confined to those regions where water ice is thermally stable.

REFERENCES AND NOTES

1. K. Watson, B. C. Murray, H. Brown, *J. Geophys. Res.* **66**, 1598 (1961); *ibid.*, p. 3033.
2. J. R. Arnold, *ibid.* **84**, 5659 (1979).
3. R. R. Hodges, *Proc. Lunar Planet Sci. Conf.* **11**, 2463 (1980).
4. G. E. Thomas, *Science* **183**, 1197 (1974).
5. M. A. Slade, B. J. Butler, D. O. Muhleman, *ibid.* **258**, 635 (1992).
6. J. K. Harmon and M. A. Slade, *ibid.*, p. 640.
7. B. J. Butler, D. O. Muhleman, M. A. Slade, in preparation.
8. S. Soter and J. Ulrichs, *Nature* **214**, 1315 (1967).
9. R. Landau, *Icarus* **52**, 202 (1982). The distribution of spectrally integrated brightness across the solar disk was approximated with formulas provided in C. W. Allen, *Astrophysical Quantities* (Athetone, London, ed. 2, 1963).
10. S. J. Peale, in *Mercury*, F. Vilas, C. R. Chapman, M. S. Matthews, Eds. (Univ. of Arizona Press, Tucson, 1988), pp. 461–493.
11. J. D. Anderson *et al.*, *Icarus* **71**, 337 (1987).
12. K. P. Klaasen, *ibid.* **28**, 469 (1976).
13. *The Astronomical Almanac* (U.S. Naval Observatory, Washington, DC, 1991).
14. S. C. Chase, E. D. Miner, D. Morrison, G. Munch, G. Neugebauer, *Icarus* **28**, 565 (1976).
15. J. Veverka, P. Helfenstein, B. Hapke, J. D. Goguen, in (*10*), pp. 37–58.
16. C. J. Cremers and R. C. Birkebak [*Proc. Lunar Planet. Sci. Conf.* **2**, 2311 (1971)] measured the thermal conductivity k of sample 10084 of lunar fines from Apollo 11 under vacuum conditions at temperatures T ranging from 200 to 400 K and found that the equation $k = 1.42 \times 10^{-3} + 1.73 \times 10^{-11} T^3$ (W m^{-1} K^{-1}) best fit the data. We used measurements of the heat capacity c of this same sample at temperatures ranging from 95 to 348 K [K. Horai and G. Simmons, in *Thermal Characteristics of the Moon*, J. W. Lucas, Ed. (MIT Press, Cambridge, 1972), pp. 243–268] and found a linear fit to the data using the equation $c = 0.0005(T - 80.0) + 0.07$ (J kg^{-1} K^{-1}). We modeled the subsurface as 40 layers with increasing thicknesses down to several annual skin depths. Subsurface temperatures were initialized with the use of estimated annual average surface temperatures and the assumed heat flow rate. Temperatures and thermal properties were recalculated every 1/1000 of a Mercury year, which corresponds to a time step of 2.11 hours.
17. G. Schubert, M. N. Ross, D. J. Stevenson, T. Spohn, in (*10*), pp. 429–460.
18. C. E. Bryson III, V. Cazcarra, L. L. Levenson, *J. Chem. Eng. Data* **19**, 107 (1974).
19. I. Esterman, *High Speed Aerodynamics and Jet Propulsion*, vol. 1 of *Thermodynamics and Physics of Matter*, F. D. Rossini, Ed. (Princeton Univ. Press, Princeton, NJ, 1955), pp. 742–744.
20. One complication is that water vapor ballistically deposited on a surface with a temperature <130 K forms amorphous ice [A. Kouchi, *Nature* **330**, 550 (1987); *J. Cryst. Growth* **99**, 1220 (1990)]. The vapor pressure of this form of ice can be orders of magnitude larger than that of crystalline ice at the same temperature and is sensitive to both the temperature and rate of accumulation during condensation. However, amorphous ice is metastable and will crystallize into the cubic phase at a temperature-dependent rate determined experimentally to follow $t_c = 9.54 \times 10^{-14}\, e^{(5370/T)}$, where t_c is the time in seconds for complete crystallization at temperature T [S. Espinasse, J. Klinger, C. Ritz, B. Schmitt, *Icarus* **92**, 350 (1991); B. Schmitt, S. Espinasse, R. J. A. Grim, J. M. Greenberg, J. Klinger, *Eur. Space Agency Spec. Publ. 302* (1989), p. 65]. Using this exponential activation law, we calculated that the time necessary for the complete crystallization of amorphous ice at 112 K is ~2 years and that ~0.05 mm of amorphous ice could sublimate in that time. If this activation law holds for lower temperatures, it would take on the order of 1 billion years for amorphous ice to crystallize completely at 78 K. However, it has been suggested that pressure crystallization might severely limit the volume fraction of amorphous ice in deep deposits (*7*).
21. S. G. Warren, *Rev. Geophys. Space Phys.* **20**, 67 (1982).
22. S. W. Squyres and J. Veverka, *Icarus* **50**, 115 (1982).
23. A. P. Lane and W. M. Irvine, *Astrophys. J.* **78**, 794 (1973).
24. M. E. Davies, S. E. Dwornik, D. E. Gault, R. G. Strom, *Atlas of Mercury* (SP-423, National Aeronautics and Space Administration, Washington, DC, 1978).
25. A. S. Adjoran, *J. Space Rockets* **7**, 378 (1970).
26. T. Svitek, thesis, California Institute of Technology, Pasadena (1992).
27. R. J. Pike, in (*10*), pp. 165–273.
28. J. I. Lunine, *Icarus* **81**, 1 (1989).

29. We thank B. J. Butler, J. K. Harmon, D. O. Muhleman, and M. A. Slade for sharing their Mercury radar results with us before publication and for many helpful discussions. Supported by the National Aeronautics and Space Administration Planetary Geology and Geophysics Program.

3 June 1992; accepted 30 July 1992

Biological Weighting Function for the Inhibition of Phytoplankton Photosynthesis by Ultraviolet Radiation

John J. Cullen,* Patrick J. Neale, Michael P. Lesser

Severe reduction of stratospheric ozone over Antarctica has focused increasing concern on the biological effects of ultraviolet-B (UVB) radiation (280 to 320 nanometers). Measurements of photosynthesis from an experimental system, in which phytoplankton are exposed to a broad range of irradiance treatments, are fit to an analytical model to provide the spectral biological weighting function that can be used to predict the short-term effects of ozone depletion on aquatic photosynthesis. Results show that UVA (320 to 400 nanometers) significantly inhibits the photosynthesis of a marine diatom and a dinoflagellate, and that the effects of UVB are even more severe. Application of the model suggests that the Antarctic ozone hole might reduce near-surface photosynthesis by 12 to 15 percent, but less so at depth. The experimental system makes possible routine estimation of spectral weightings for natural phytoplankton.

Declines in the concentration of stratospheric O_3 (*1*), particularly in the Antarctic during the austral spring (*2*), result in more UVB radiation reaching the earth's surface (*3*) and the upper part of aquatic photic zones (*4*, *5*). Environmental UVB is harmful to many biological processes (6–9), so intense efforts have been made to assess the photobiological effects of stratospheric O_3 depletion (6). Biological effects of absorbed ultraviolet radiation (UV) are generally a function of wavelength; therefore, they are best quantified with a spectral biological weighting function (*3*, *7*, *8*). The weighting function, comparable to an action spectrum (*7*, *9*), should accommodate interactions between (i) the UV that damages photosynthetic processes and (ii) longer wavelengths, which activate processes that counteract the damage (*4*, *10*). That is, photoinhibition is likely to be a function of both UV and the ratio between UV and photosynthetically active radiation (PAR, 400 to 700 nm) (*11*). A good model of spectral dependence is particularly important for studies of aquatic photosynthesis, because both UV and the ratio UV:PAR change with depth in the water column (*5*).

We constructed an analytical model of photosynthesis to describe the interaction

J. J. Cullen, Department of Oceanography, Dalhousie University, Halifax, Nova Scotia, Canada B3H 4J1, and Bigelow Laboratory for Ocean Sciences, McKown Point, West Boothbay Harbor, ME 04575.
P. J. Neale, Department of Plant Biology, University of California, Berkeley, CA 94720, and Bigelow Laboratory for Ocean Sciences, McKown Point, West Boothbay Harbor, ME 04575.
M. P. Lesser, Bigelow Laboratory for Ocean Sciences, McKown Point, West Boothbay Harbor, ME 04575.

*To whom correspondence should be addressed.